ADVANCED MATERIALS
www.advmat.de

Sequential Co-Passivation in InAs Colloidal Quantum Dot Solids Enables Efficient Near-Infrared Photodetectors

*Pan Xia, Bin Sun, Margherita Biondi, Jian Xu, Ozan Atan, Muhammad Imran, Yasser Hassan, Yanjiang Liu, Joao M. Pina, Amin Morteza Najarian, Luke Grater, Koen Bertens, Laxmi Kishore Sagar, Husna Anwar, Min-Jae Choi, Yangning Zhang, Minhal Hasham, F. Pelayo García de Arquer, Sjoerd Hoogland, Mark W. B. Wilson, and Edward H. Sargent**

III-V colloidal quantum dots (CQDs) are promising materials for optoelectronic applications, for they avoid heavy metals while achieving absorption spanning the visible to the infrared (IR). However, the covalent nature of III-V CQDs requires the development of new passivation strategies to fabricate conductive CQD solids for optoelectronics: this work shows herein that ligand exchanges, previously developed in II-VI and IV-VI quantum dots and employing a single ligand, do not fully passivate CQDs, and that this curtails device efficiency. Guided by density functional theory (DFT) simulations, this work develops a co-passivation strategy to fabricate indium arsenide CQD photodetectors, an approach that employs the combination of X-type methyl ammonium acetate (MaAc) and Z-type ligands $InBr_3$. This approach maintains charge carrier mobility and improves passivation, seen in a 25% decrease in Stokes shift, a fourfold reduction in the rate of first-exciton absorption linewidth broadening over time-under-stress, and leads to a doubling in photoluminescence (PL) lifetime. The resulting devices show 37% external quantum efficiency (EQE) at 950 nm, the highest value reported for InAs CQD photodetectors.

1. Introduction

The recent development of technologies relying on sensitive and fast photodetectors, such as light detection and ranging (LiDAR), has further increased interest in high-performing and cost-effective infrared (IR) optoelectronics materials. III-V colloidal quantum dots (CQDs) have received increasing attention.[1–4] InAs CQDs are of particular interest due to their low permittivity, large exciton Bohr radius, tunable absorption into IR, and ease of solution-processing onto a substrate. However, the covalent nature of In-As brings new challenges compared to well-developed PbS CQDs, the latter characterized by ionic bonding.[5–7]

Surface defect-induced trap states in III-V CQDs are thought to reside deeper in the bandgap than those in ionic CQDs, damaging device performance.[6,8] To passivate

P. Xia, M. Biondi, J. Xu, O. Atan, M. Imran, Y. Liu, J. M. Pina, A. M. Najarian, L. Grater, K. Bertens, L. K. Sagar, H. Anwar, Y. Zhang, S. Hoogland, E. H. Sargent
Department of Electrical and Computer Engineering
University of Toronto
10 King's College Road, Toronto, ON M5S 3G4, Canada
E-mail: ted.sargent@utoronto.ca

M. Hasham, M. W. B. Wilson
Department of Chemistry
University of Toronto
80 St. George Street, Toronto, ON M5S 3H6, Canada

B. Sun
Key Laboratory for Organic Electronics and Information Displays
Institute of Advanced Materials (IAM)
Nanjing University of Posts and Telecommunications
Nanjing 210023, China

Y. Hassan
Department of Chemistry and Earth Sciences
College of Arts and Sciences
Qatar University
PO Box: 2713, Doha Qatar

M.-J. Choi
Department of Chemical and Biochemical Engineering
Dongguk University
Seoul 04620, Republic of Korea

F. P. G. de Arquer
ICFO–Institut de Ciències Fotòniques
The Barcelona Institute of Science and Technology
08860 Castelldefels, Barcelona Spain

The ORCID identification number(s) for the author(s) of this article can be found under https://doi.org/10.1002/adma.202301842

DOI: 10.1002/adma.202301842

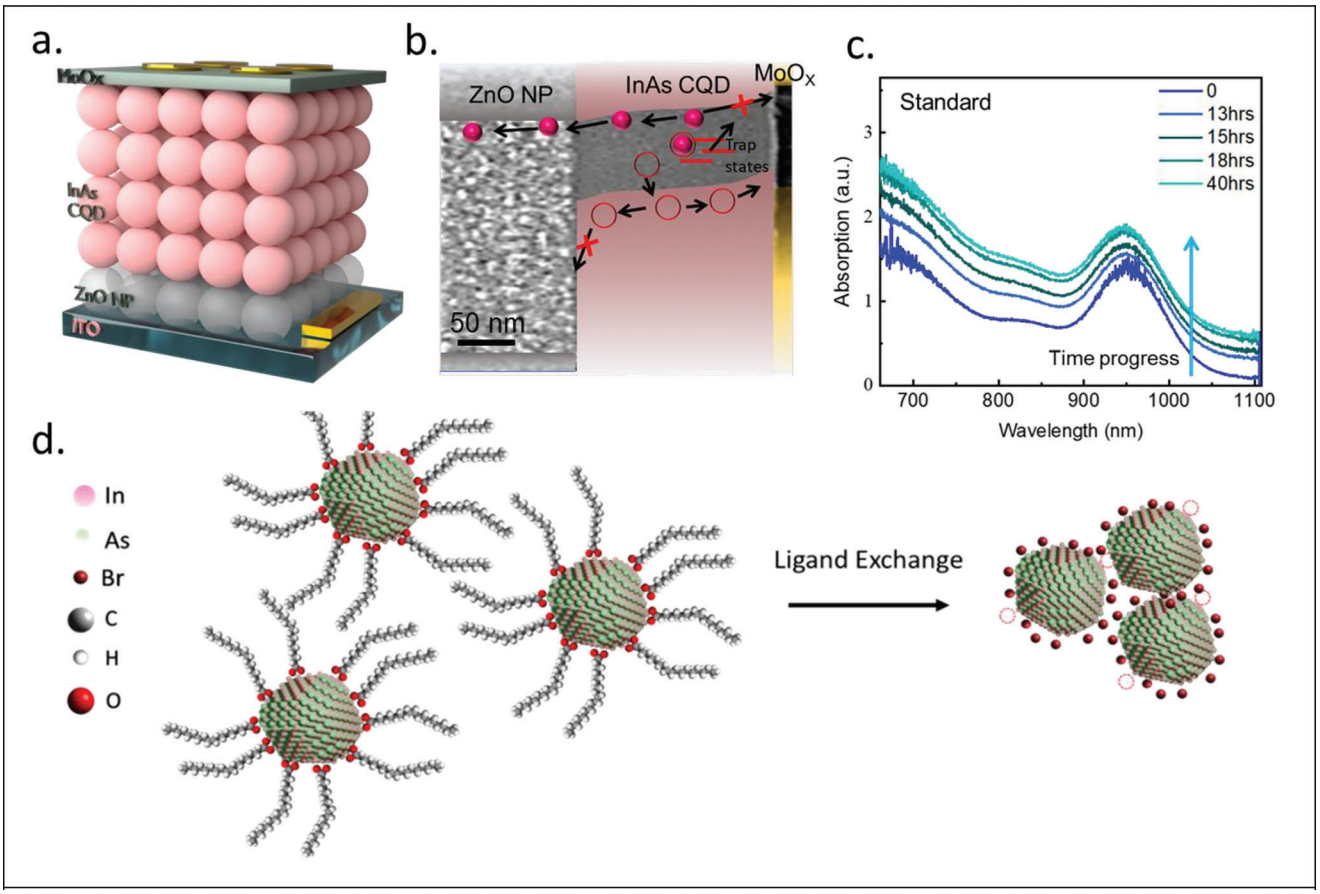

Figure 1. a) InAs colloidal quantum dot (CQD) photodetector: a ZnO electron transport layer (ETL), the InAs absorber layer, a MoO_x hole transport layer (HTL), and a silver contact (with device cross-section as background). b) Charge transport and effect of defects in an InAs photodiode; c) colloidal stability of InAs CQD with standard ligand exchange strategy as a function of storage time. d) Standard InAs CQD ligand exchange.

III-V CQD, strategies such as growing a thicker shell (e.g., CdS, CdSe, ZnS, or ZnSe),[9–11] etching the surface with acid,[1,8] and introducing doping elements such as zinc and cadmium[1,12] have been utilized.[9–11] However, these strategies either block carrier extraction or are uncontrollable, resulting in more surface defects and decreasing size homogeneity.

Recent studies have advanced the synthesis of InAs CQDs, providing improved passivation to create conductive films in optoelectronic devices.[1,13–16] Current InAs QD photodiodes employ a one-step ligand exchange that substitutes long insulating oleic acid (OA) ligands with short Z-type ligands, metal halides, or L-type ligand thiols.[5,13] However, the charge collection efficiency of these devices is limited, leading to an external quantum efficiency (EQE) below 30% without bias. The low charge collection may be assignable to incomplete passivation of III-V CQD surfaces; as seen in InP and PbS CQDs, halides alone do not fully passivate the surface, and suboptimal passivation causes defects in an active photodetector layer made from these dots.[16–18]

In this work, we focused on developing a new ligand exchange strategy that can improve InAs CQD passivation, increase colloidal stability, and thus device performance. We first applied first-principles density functional theory (DFT) calculations to find that co-passivation of acetate with halides reduced traps within the bandgap. To maximize passivation and minimize competition between the halide and the acetate anchoring group of methylammonium acetate (MaAc) ligand, we introduce the X-type ligand MaAc during a second passivating step after the standard halide exchange as a co-passivation strategy. Co-passivation reduces CQD surface defects, decreasing Stokes shift by 25% and doubling photoluminescence (PL) lifetime. The resulting InAs CQD inks show a factor of 4.4 times improvement in stability as a result of improved passivation. The increased surface passivation also enables a 20% increase in EQE compared to the previous best and a twofold increase in sensitivity compared to the control devices.

2. Results and Discussion

InAs photodetectors are fabricated using a p-i-n junction, as in **Figure 1**a. Given the complexity and covalent nature of the InAs CQD surface, tailoring a ligand exchange that removes long-chain OA ligands and retains passivation while minimizing defects in the active layer is challenging. To address this passivation issue, we previously reported substituting the original OA ligands with $InBr_3$, resulting in high carrier mobility InAs CQD film.[13] After ligand exchange, bromide-passivated conductive CQD solids can be employed in optoelectronic devices. However, the EQE of InAs CQD photodetectors is still limited to 30% at

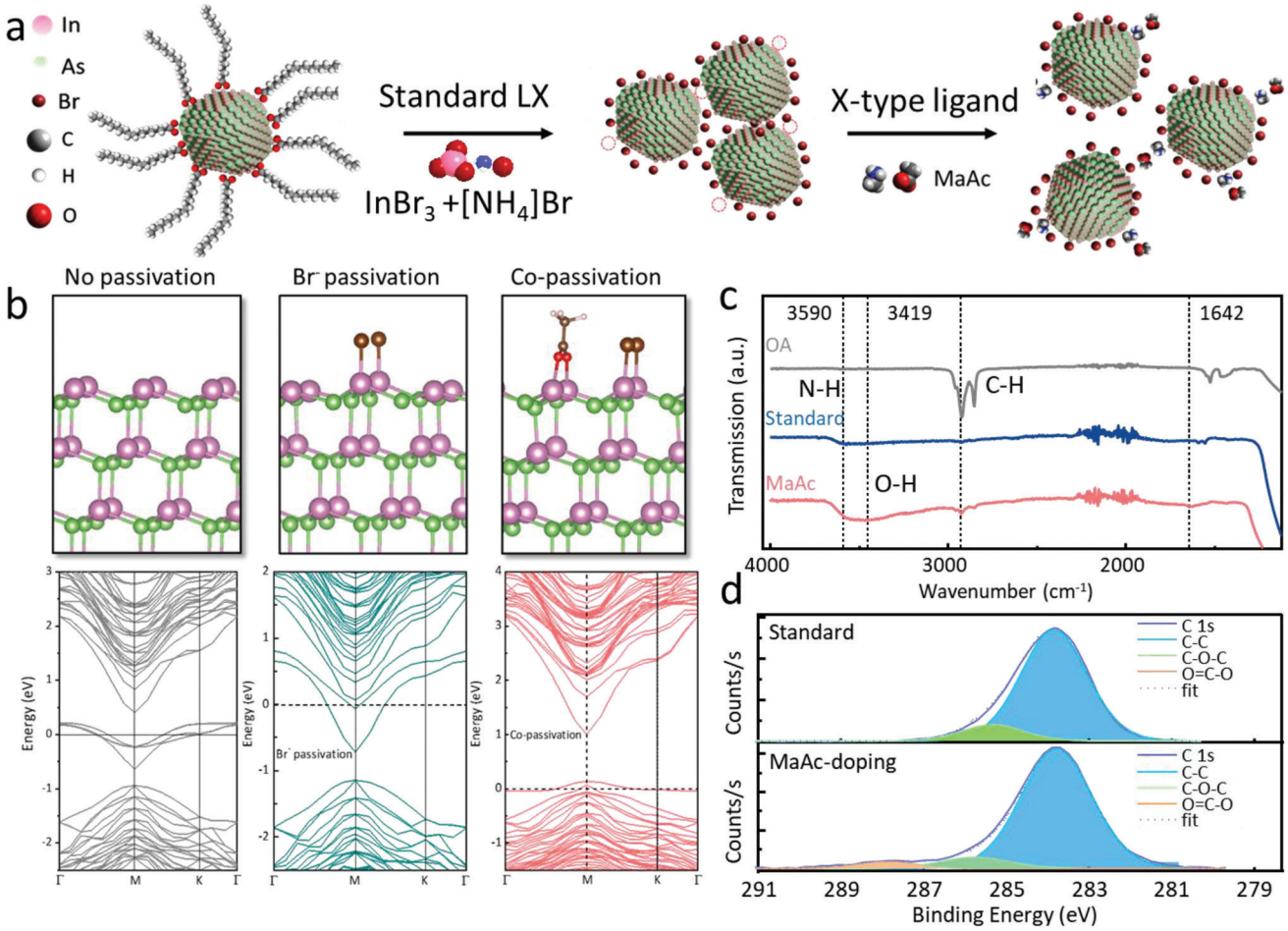

Figure 2. a) Ligand exchange protocol with the addition of methyl ammonium acetate (MaAc) passivation. b) density functional theory (DFT) simulation, side views of ball-and-stick models on InAs (111) facet with naked, pure Br^-passivation and co-passivation with Br^- and acetate, and their respective band structures near the Fermi energy (dash line). c) Fourier-transform infrared spectroscopy (FTIR) measurements of as-synthesized and exchanged InAs colloidal quantum dot film with standard and MaAc exchange (MaAc-doped). d) X-ray photoelectron spectroscopy (XPS) spectra of carbon 1s of standard and MaAc-doped CQD solids.

950 nm, and the dark current density is around 10^2 nA cm^{-2} at 1 V bias. At the same time, commercial fast-response silicon can reach 1 nA cm^{-2}.[19] Notably, as the reverse bias increased, the dark current increased. This result agrees with prior studies indicating that trap density and band-band tunneling for low bandgap materials are major sources of high dark current.[20] The band-to-band tunneling is caused by improper band alignment or the loss of a built-in field.

We sought to overcome this by optimizing the hole transporting layer (HTL)/active layer (MoO_x and InAs) and electron tranporting layer (ETL)/active layer (ZnO NP and InAs) interfaces. However, our attempts failed and either decreased EQE or increased dark current, which implies that defects in the active layers result in undesirable recombination, leading to a large dark current, low detectivity, and a low EQE (Figure 1b and Figure S2, Supporting Information). The Solar Cell Capacitance Simulator (SCAPS-1D) simulation indicates that CQD's trap density and doping level heavily affect EQE and dark current (Figure S1, Supporting Information). We attribute this to the insufficient passivation of CQD and subsequent agglomeration after the ligand exchange. In addition, the poor colloidal stability of CQD following ligand exchange, indicated by absorption changes, confirmed this (Figure 1c,d).[13,21,22]

These findings pointed us to focus on passivation for InAs CQDs to reduce defect density, thus improving photodetector performance. We started the ligand exchange with a pure Z-type ligand, $InBr_3$, which prior studies showed provides good passivation, and the X-type ligand ammonium bromide (NH_4Br) to maintain the anion-cation stoichiometric ratio and balance the CQD charge after ligand exchange.[13] Even so, the colloidal stability of CQD remains a concern, as CQD precipitated as time progressed (Figure 1c). We simulated, using DFT, the effect of CQD passivation as a function of various ligand combinations (**Figure 2**b). These studies estimated that the binding energy of the acetate group is ≈0.6 eV higher than that of Br on InAs (111) facets (Figure S3, Supporting Information). Thus, an X-type ligand with a higher binding affinity, such as acetate, could be the optimal choice. In addition, the band structures predicted by DFT simulations reveal that by adding acetate to the Br-passivated InAs (111) facet, the trap states can be substantially reduced due

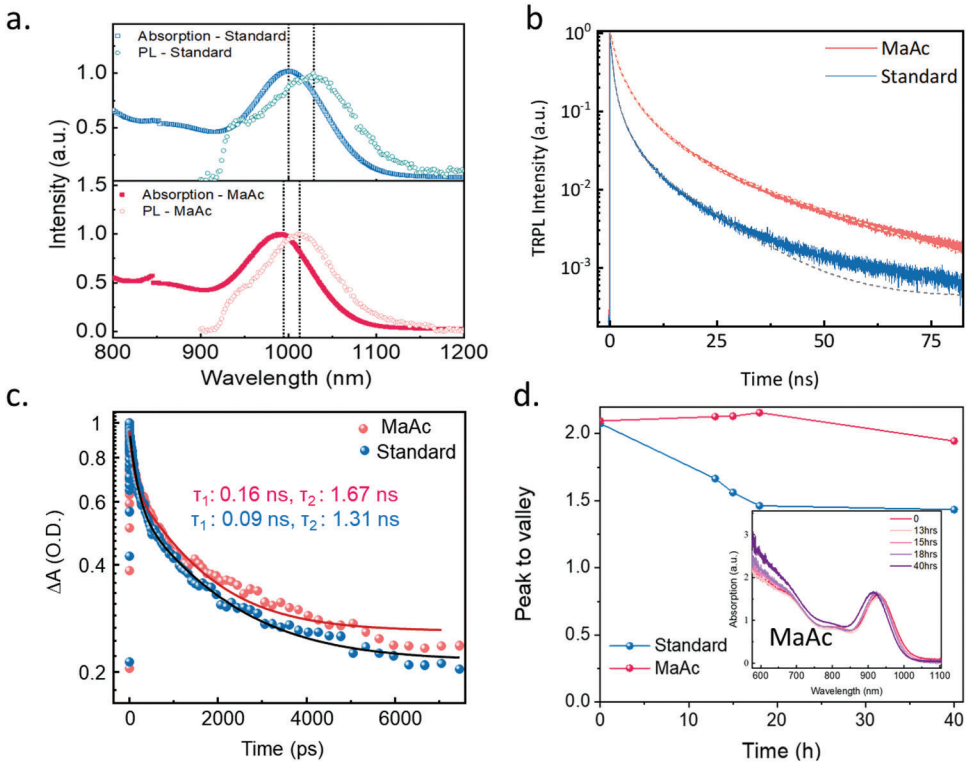

Figure 3. a) Stokes shift measurements of InAs colloidal quantum dot (CQD) inks. b) Time-resolved photoluminescence (TRPL) measurements of InAs CQD ink solution (solid line, fit; the current fitting models probe the 99.5% decay). c) Transient absorption (TA) measurements of InAs CQD in solution (560 nm excitation with 0.11 mJ cm^{-2} $pulse^{-1}$ fluence). A biexponential fit is applied, suggesting a fast and a slow decay component. d) Ink stability of InAs CQDs from standard and methyl ammonium acetate (MaAc) doped ligand exchange.

to reduced dangling electronic states in the band gap region.[18]

Experimentally, MaAc has previously been reported as a passivation reagent in perovskite solar cells, leading to decreased defects and improved interfaces with metal oxide nanoparticle ETLs.[23] MaAc can bind to the vacant sites of the III-V CQDs, given that a small positive ammonium ion and negative acid moiety would make an efficient co-passivation of the CQDs.[18,24] Hence, to maximize the effect of co-passivation, we introduce MaAc in the final-step solution ligand exchange to treat the unpassivated surface sites leftover after the standard $InBr_3/NH_4Br$ exchange step, see schematics summarizing the ligand exchange reaction in Figure 2a. We compare the results of InAs CQDs capped with MaAc (MaAc-doped) to those of InAs CQDs samples (standard)—without adding MaAc, to study the effect of the co-passivation.

Fourier-transform infrared spectroscopy (FTIR) and X-ray photoelectron spectroscopy (XPS) were used to characterize the surfaces of InAs CQD before and after ligand exchange. FTIR spectra of the MaAc-doped sample show distinct features at 3419 cm^{-1}, attributed to O–H stretch of –COOH, and multipeak at 2950–2850 cm^{-1}, attributed to C–H stretch of $[CH_3NH_3]^+$ and acetate (Figure 2b). These features are absent in oleate-capped and pure $InBr_3$-exchanged CQDs, suggesting MaAc on the CQD surface. XPS results on exchanged solids show the carboxylate (COO^-) peak in the carbon-1s spectrum at 286.8 eV for MaAc-doped CQDs, confirming MaAc on the CQD surface (Figure 2c,d). Figure S6c (Supporting Information) shows the indium-3d XPS spectra of MaAc-doped CQDs with reduced peak broadness, demonstrating that enhanced passivation can reduce indium oxide formation, which widens the XPS spectra.[5] MaAc-doped samples have a lower binding energy level of arsenide than standard samples, suggesting a rise in electron density and more neutral arsenic (III) (Figure S6, Supporting Information).

To better understand our sequentially co-passivated MaAc-doped CQDs, we measured PL and absorbance on CQD inks before (standard CQDs) and after adding the MaAc ligand. Stokes shift indicates defects in CQDs, as intrabandgap trap states cause redshift emission.[25] In the MaAc-doped CQDs, the Stokes shift decreases by 25% compared to standard CQDs, suggesting a decrease in the defect density of the CQD surface (**Figure 3**a).

We performed time-resolved photoluminescence (TRPL, Figure 3b) on standard CQD ink and MaAc-doped InAs CQDs to investigate exciton decay with different passivation. Co-passivation increases the intensity-weighted lifetime PL of InAs CQD from 4.83 to 9.36 ns (Figure S8e and Table S1, Supporting Information) and slightly increases the relative PL (Figure S8f, Supporting Information). This increased lifetime arising from MaAc doping relative to the standard ink is shorter than previously observed for InAs CQDs with native OA passivation or capped with a CdS/ZnS shell.[9,12,26] The decay occurring within a few hundred picoseconds has been eliminated. Such an increase in PL lifetime and elimination of the fast decay component indicates better surface passivation of MaAc-doped InAs CQDs than the standard CQDs. The standard sample demonstrates a more

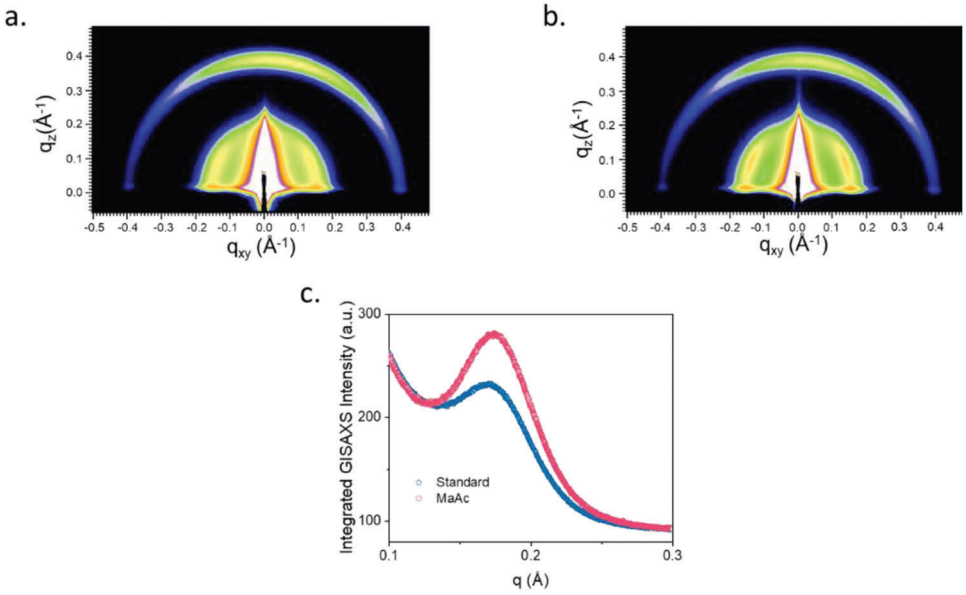

Figure 4. a) Grazing-incidence small-angle X-ray scattering (GISAXS) spectra of methyl ammonium acetate (MaAc) doped InAs colloidal quantum dot (CQD) solids. b) GISAXS pattern of standard InAs CQD solids. c) Integrated GISAXS intensity for standard and MaAc-doped InAs CQD solids.

rapid PL decay, indicating nonemissive recombination through trap states. These results agree with XPS results and Stokes shift observations.

We investigated the effect of co-passivation on carrier dynamics processes using transient absorption (TA) spectroscopy.[27] After ligand exchange, standard and MaAc-doped InAs CQDs are redispersed in the mixture solvent and excited with 560 nm pump light to monitor the ground state bleach (GSB) of CQDs close to exciton peaks. The dynamics are extracted at the exciton peaks and plotted in Figure 3c (Figure S8, Supporting Information). Fitting shows two decay components, the 100-ns scale, and the 1-ns scale, in agreement with reported lifetimes (Table S2, Supporting Information).[13] The TA results show that the GSB rate is 1.2 times slower in MaAc-doped CQDs than in standard CQDs, suggesting a decrease in surface electron trap states.[28,29] These findings and a smaller Stokes shift show better surface passivation of the CQDs after MaAc treatment.

We then monitor the ligand exchanged CQD absorption under nitrogen to study the colloidal stability. We found that the absorption spectra of MaAc-doped CQDs show no noticeable changes upon aging (up to 40 h). In contrast, the absorption features of standard CQDs vary significantly over the same time span (Figure 3d). The peak-to-valley (P2V) ratio of the first exciton peak of MaAc-doped CQD inks decreased by 7%, while the standard InAs ink decreased by 31%, suggesting that MaAc-capped CQDs are less likely to aggregate.

To study the effect of co-passivation on the ordering of CQD in solid films, we performed grazing-incidence small-angle X-ray scattering (GISAXS) on as-synthesized CQDs (Figure S8, Supporting Information), InAs CQD solids after standard ligand exchange (Standard) (**Figure 4**a), and the MaAc ligand exchange (MaAc-doped) (Figure 4b). After ligand exchange, the interdot distance decreases from 4.4 to 3.7 nm for the standard sample to 3.6 nm for the MaAc-doped sample, and the peak broadness decreases. We attribute this to a better overall packing of the CQD solids. Better packing and ordering of the MaAc-doped InAs solids are also shown by the increase in peak-to-valley ratio in the integrated GISAXS peaks (Figure 4c).

Dark currents of hole-only and electron-only devices were tested to study CQD film mobility and trap density with and without MaAc surface passivation. The space charge limited current (SCLC) regime estimates mobility, while the trap-filled regime estimates trap density. Though the electron and hole mobilities were nearly maintained, the trap density was significantly reduced after the surface passivation with the MaAc (Figure S10, Supporting Information). The quantitative comparison shows the decrease in electron trap densities by 80% and hole trap densities by 50%.

Given the promising results of CQD inks, we used MaAc-doped InAs CQD solids to fabricate the near-infrared photodetector. We compared it to the best photodiodes using single-step $InBr_3$ exchange (control devices).[11] MaAc-doped CQD devices (denoted as MaAc devices) show a decrease in the dark current; in particular, when the detector is at reverse bias (−0.5 and −1 V), one order of magnitude decrease in the dark current is seen in MaAc-doped devices (6.7×10^{-6} and 9.2×10^{-6} A cm^{-2} for control). Ultraviolet photoelectron spectroscopy (UPS) shows the MaAc-doped InAs CQD films are 0.2 eV more intrinsic than the standard sample (Figure S11, Supporting Information), which is heavily n-doped with a carrier concentration of 10^{17} cm^{-3}.[13] Meanwhile, SCAPS shows that dark current is sensitive to InAs CQD doping and trap density, a lower doping level and lower trap density, and thus a higher EQE and a lower dark current (Figure S1, Supporting Information). Therefore, lower dark current results from a decreased doping level of CQD and better dot arrangement in film, which are both affected by the ligand exchange strategy (**Figure 5**a).

MaAc-doped devices also show an increase in EQE to 37% at 0 V, which is a ≈20% improvement compared to the best previous InAs CQD photodetector (Figure 5b).[13] EQE increases due

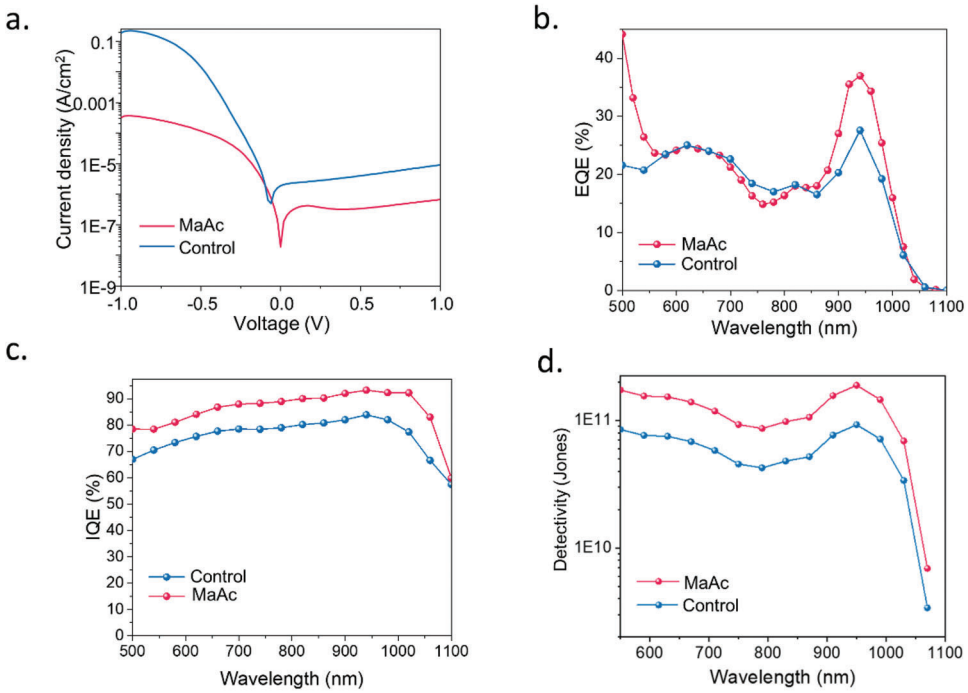

Figure 5. Photodetector performance. a) Dark current; b) external quantum efficiency (EQE); c) internal quantum efficiency (IQE); d) detectivity of InAs colloidal quantum dot (CQD) photodetectors.

to more efficient charge extraction and a decrease in InAs trap density. The former can be seen from the internal quantum efficiency (IQE) values. IQE is the ratio between charges absorbed and charges collected in the devices. It reaches ≈95% of the excitonic peak for MaAc-doped devices, a 10% improvement compared to the control (Figure 5c). SCLC and SCAPS show that the decrease in the doping level and the trap density contributed to the increase in EQE (Figures S1 and S10, Supporting Information).

To study the sensitivity of the photodetector, we measured the noise current (Figure S12, Supporting Information) and calculated the device's detectivity. The MaAc-doped devices show an improved sensitivity with 1.9×10^{11} Jones detectivity at 950 nm (at 10 kHz), a 100% improvement compared to the standard sample (0.9×10^{11} Jones). An increase in sensitivity is enabled by a decrease in defects in the active layer and decreased recombination of the device, which results in a lower noise current. Moreover, we noticed the dark current was maintained for 17 h for the MaAc-doped device (Figure S13, Supporting Information). Transient photocurrent responses of control and MaAc-doped devices with 0.098 cm^2 pixel size at 0 bias show 1.0 µs rise and 1.4 µs fall times (Figure S14, Supporting Information). Although our photodetectors show enhanced performances (Table S3, Supporting Information), their detectivity still lags behind the commercially available InGaAs photodetectors.[30] Therefore, further efforts are needed for the InAs CQD-based photodetector prior to its use in consumer electronics.

In sum, we developed an efficient sequential ligand strategy for InAs CQDs. Employing X- and Z-type ligands-based co-passivation strategy (MaAc, NH_4Br, and Z-type ligands, $InBr_3$) improves the passivation of III-V CQD, resulting in better colloidal stability. This enabled us to fabricate a highly efficient Pb-free CQD-based photodetector, achieving a record EQE of 37% at 950 nm and doubling the detectivity to 1.9×10^{11} Jones. This co-passivation strategy provides guidance for the surface passivation design of III-V CQD surfaces with additional covalency for optoelectronic applications.

3. Experimental Section

CQD Synthesis: OA capped InAs CQDs with the first excitonic peak at 950 nm (1.31 eV) were synthesized using a continuous injection by reacting $In(oleate)_3$, tris(trimethylgermyl)arsine ($(TMGe)_3As$) under an N_2 atmosphere at 300 °C using a modified approach.[16,31]

Synthesis of Control CQD Inks: Control devices were fabricated following an existing procedure.[3] The $InBr_3$/AA solution-phase ligand exchange process was carried out in a test tube in an N_2-filled glovebox. $InBr_3$ (0.1 mol L^{-1}, 0.18 g) and AA (ammonium acetate) (0.04 mol L^{-1}, 0.023 g) were predissolved in 5 mL of DMF. About 1 mL of CQD octane solution (10 mg mL^{-1}) was added to 5 mL of the precursor solution. These were vortexed for 1–2 min until the CQDs were completely transferred to the DMF phase, followed by washing three times with octane. After ligand exchange, CQDs were precipitated by adding toluene (≈10 mL) and separated by centrifugation. After 10 min of vacuum drying, the CQDs were redispersed in DMF (200 mg mL^{-1}) and spin-coated at 2000 rpm.

Synthesis of Standard CQD Ink: The $InBr_3$/ABr solution-phase ligand exchange process was carried out in a test tube in an N_2-filled glovebox. $InBr_3$ (0.049 mmol, 0.175 g) and NH_4Br (0.077 mmol, 0.0375 g) were predissolved in 5 mL of DMF. About 1 mL of CQD octane solution (10 mg mL^{-1}) was added to 5 mL of the precursor solution. These were vortexed for 1–2 min until the CQDs were transferred entirely to the DMF phase, followed by washing three times with hexane. After ligand exchange, CQDs were precipitated by adding acetone (≈10 mL) and separated by centrifugation. After 10 min of vacuum drying, CQD solid

dissolves in $InBr_3$ (0.1 mol L^{-1}, 0.105 g) and ammonium bromide (0.077 mol L^{-1}, 0.022 g) GBL:DMSO = 1:2 solvent. These were vortexed for 90 sec until the CQDs were wholly dissolved, followed by precipitating by adding acetone (≈0.8 mL) and centrifugation. After 10 min of vacuum drying, the CQDs were redispersed in a solution of MaAc in a mixture of DMSO, GBL, and acetonitrile to form MaAc doped ink or without MaAc in DMSO, GBL, and acetonitrile mixture to form standard procedure without MaAc ink. After the exchange, the CQDs were precipitated again using acetone, dried for 5 min, and spin-coated at 2000–5000 rpm (250 g mL^{-1}).

CQD Photodetector Fabrication: The ZnO nanoparticles were synthesized using a published method.[32]The ZnO nanoparticles were spin-cast on an ITO substrate at 5000 rpm for 20 s (2 layers, ≈150 nm thickness). CQD ink was used to fabricate devices. The CQD films were spin-cast (at 2000 rpm) on the ZnO/ITO substrate with a 200–250 mg mL^{-1} concentration of the CQD inks. Finally, 14 nm of MoO_x was deposited as HTL, and 120 nm of Au was thermally deposited as a back electrode.

TPC Measurement: The temporal response of the photodetectors was recorded using a 1-GHz oscilloscope (Oscilloscope, Tektronix). An 850 nm vertical-cavity surface-emitting laser (VCSEL) modulated at a frequency of 20 kHz using a function generator (Tektronix, AFG31000) was used to illuminate the pixels. The photodetector signal was preamplified (10^3 V A^{-1}) using a preamplifier (Femto DHPCA-100). The photodetector was biased through the preamplifier when applicable.

Dark Current and EQE Measurement: Current–voltage characteristics were measured with a Keithley 2400 source in dark conditions. Devices were tested under a continuous nitrogen flow. The *I–V* curves were scanned from −1.0 to +1.0 V at 0.02 V interval steps. EQE spectra were taken by subjecting the devices to chopped (220 Hz) monochromatic illumination (a 400 W Xenon lamp passing through a monochromator and appropriate cutoff filters). Newport 818-UV and Newport 838-IR photodetectors were used to calibrate the output power. The response of the devices was measured with a Lakeshore preamplifier feeding into a Stanford Research 830 lock-in amplifier under short-circuit conditions.

IQE Calculation: IQE values are calculated by dividing the EQE at 0 V by the biased EQE at −1 V.[33]

Noise Equivalent Power measurement and Specific Detectivity Calculation: The noise spectra were measured using a signal analyzer (N9010A, Agilent) combined with a low-noise preamplifier. Noise measurements were carried out in the dark at room temperature for the pixels with a 0.1 cm^2 area. The noise current was calculated using the noise signal measured at 10 kHz and an amplification of 10^6 V A^{-1} from the preamplifier. The detectivity was calculated based on noise current, responsivity, a set bandwidth of 1 Hz, and the active area.[34,35]

Space Charge Limited Current Measurements: *J–V* characteristics of hole and electron only devices were measured. The hole only device was fabricated using ITO/MoO_3/InAs CQD/MoO_3/Ag and the electron-only device was fabricated using ITO/PEIE (polyethylenimine)/InAs CQD/LiF/Ag structure. The thickness of the CQD layer was 80–100 nm.

UPS Measurements: A helium discharge source (HeI α, $h\upsilon = 21.22$ eV) was used, and the samples were kept at a take-off angle of 88°. During measurement, the sample was held at a −5 V bias relative to the spectrometer to collect low kinetic energy electrons efficiently. EF was calculated from the equation: EF = 21.22 eV − S_{EC}, where S_{EC} is the secondary electron cutoff. The difference between the valence band (VB) and EF, η, was determined from the VB onset in the VB region.

XPS Measurements: XPS measurements were carried out on CQD solids after ligand exchange. XPS measurements were carried out using a Thermo Scientific K-Alpha system with a 75 eV pass energy and binding energy steps of 0.05 eV.

FTIR Measurement: FTIR spectra were obtained using a Thermo Scientific iS50 with a spectral range of 4000–1000 cm^{-1} and an ATR accessory. Samples were prepared on glass substrates with the same thickness as photodetectors. The peaks 2000–2200 cm^{-1} were assigned to the CO_2 in the air.

PL and TRPL Measurements: PL measurements were carried out using a Horiba Fluorolog Time-Correlated Single Photon Counting system equipped with UV/Vis/NIR photomultiplier tube detectors and dual grating spectrometers. TRPL experiments were performed using a $\lambda = 470$ nm pulsed diode laser (PicoQuant, LDH-D-C-470) at 10 μJ cm^{-2} $pulse^{-1}$, and data was collected using a single photon avalanche diode (Micro Photon Devices, $PD-050-CTD) and a PicoQuant HydraHarp 400 event timer. The repetition rate of the laser was 1 MHz, and the intrinsic time resolution was 16 ps. All samples are in hexane solution with 18–20 μmol L^{-1} concentration.[36]

TA Measurements: A regeneratively amplified Yb:KGW laser with a 5 kHz repetition rate (Light Conversion, Pharos) was used to generate femtosecond laser pulses, and a pulse picker was used to lower the frequency to 1 kHz. A portion of the 1030 nm fundamental was sent into an optical bench (Ultrafast, Helios). It passed through a –1 retroreflector and was then focused into a calcium fluoride crystal, translated at 1 mm to create the white light continuum probe. An optical parametric amplifier (Light Conversion, Orpheus) generated the 560 nm pump pulse by upconverting the fundamental wavelength. This was then sent to the optical bench and chopped at 500 Hz. Both the pump and probe were sent to the sample, with the time delay adjusted by changing the path length of the probe (time resolution ≈350 fs). A CCD detector collected the probe pulse after dispersion by a grating spectrograph (ultrafast). Kinetic traces were fitted to the convolution of the instrument response and a sum of exponential decay. Time zero was allowed to vary with wavelength to account for the chirp of the probe.

Computational DFT Simulation: We performed DFT calculations with Vienna Ab-Initio Simulation Package (VASP).[37]The generalized gradient approximation of Perdew–Burke–Ernzerh (PBE)[38] and the screened Heyd–Scuseria–Ernzerhof (HSE06) hybrid functional [39,40] were adopted for the exchange-correlation function. A plane-wave basis set with a kinetic energy cutoff of 400 eV was used. To simulate In-rich (111) InAs surfaces, we employed the (2 × 2) surface model with various passivation schemes. In our calculations of the binding energy of ligands with the InAs surface, we used the 4 × 4 surface model. Different adsorption sites of ligands on InAs surfaces were considered, including In-top, As-top, and hollow sites. The dipole correction was included in the slab calculations. Pseudo-hydrogen atoms with 0.75 electrons were used for passivating the As-terminated back surface.

Supporting Information

Supporting Information is available from the Wiley Online Library or from the author.

Acknowledgements

P.X., B.S., and M.B. contributed equally to this work. The authors thank Larissa Levina, Elenita Palmiano, Remi Wolowiec, and Damir Kopilovic for their assistance during the study period. The authors thank Ahmet Gulsaran from the University of Waterloo for helping with the characterization of the CQD materials. The authors thank Yonghua Chen for the discussion and for providing research materials. Part of the research described in this paper was performed at the Canadian Light Source, a national research facility of the University of Saskatchewan, which is supported by the Canada Foundation for Innovation (CFI), the Natural Sciences and Engineering Research Council (NSERC), the National Research Council (NRC), the Canadian Institutes of Health Research (CIHR), the Government of Saskatchewan, and the University of Saskatchewan. Part of the XPS measurements were carried out at the CFI-funded Ontario Centre for the Characterization of Advanced Materials at the University of Toronto. Part of this work on XPS and UPS was conducted at the University of Alberta nano FAB Centre.

Conflict of Interest

The authors declare no conflict of interest.

Data Availability Statement

The data that support the findings of this study are available from the corresponding author upon reasonable request.

Keywords

III-V compound semiconductors, indium arsenide, near-infrared photodetectors

Received: February 26, 2023
Revised: May 8, 2023
Published online:

[1] J. H. Song, H. Choi, H. T. Pham, S. Jeong, *Nat. Commun.* **2018**, *9*, 4267.
[2] D. Franke, D. K. Harris, O. Chen, O. T. Bruns, J. A. Carr, M. W. B. Wilson, M. G. Bawendi, *Nat. Commun.* **2016**, *7*, 12749.
[3] Y.-H. Won, O. Cho, T. Kim, D.-Y. Chung, T. Kim, H. Chung, H. Jang, J. Lee, D. Kim, E. Jang, *Nature* **2019**, *575*, 634.
[4] H. Van Avermaet, P. Schiettecatte, S. Hinz, L. Giordano, F. Ferrari, C. Nayral, F. Delpech, J. Maultzsch, H. Lange, Z. Hens, *ACS Nano* **2022**, *16*, 9701.
[5] M.-J. Choi, L. K. Sagar, B. Sun, M. Biondi, S. Lee, A. M. Najjariyan, L. Levina, F. P. García de Arquer, E. H. Sargent, *Nano Lett.* **2021**, *21*, 6057.
[6] Y. Kim, J. H. Chang, H. Choi, Y.-H. Kim, W. K. Bae, S. Jeong, *Chem. Sci.* **2020**, *11*, 913.
[7] M. Ginterseder, D. Franke, C. F. Perkinson, L. Wang, E. C. Hansen, M. G. Bawendi, *J. Am. Chem. Soc.* **2020**, *142*, 4088.
[8] T.-G. Kim, D. Zherebetskyy, Y. Bekenstein, M. H. Oh, L.-W. Wang, E. Jang, A. P. Alivisatos, *ACS Nano* **2018**, *12*, 11529.
[9] L. K. Sagar, G. Bappi, A. Johnston, B. Chen, P. Todorović, L. Levina, M. I. Saidaminov, F. P. García de Arquer, D.-H. Nam, M.-J. Choi, S. Hoogland, O. Voznyy, E. H. Sargent, *Chem. Mater.* **2020**, *32*, 7703.
[10] R. Tietze, R. Panzer, T. Starzynski, C. Guhrenz, F. Frenzel, C. Würth, U. Resch-Genger, J. J. Weigand, A. Eychmüller, *Part. Part. Syst. Charact.* **2018**, *35*, 1800175.
[11] H. Zhang, N. Hu, Z. Zeng, Q. Lin, F. Zhang, A. Tang, Y. Jia, L. S. Li, H. Shen, F. Teng, Z. Du, *Adv. Opt. Mater.* **2019**, *7*, 1801602.
[12] D. Zhu, F. Bellato, H. Bahmani Jalali, F. Di Stasio, M. Prato, Y. P. Ivanov, G. Divitini, I. Infante, L. De Trizio, L. Manna, *J. Am. Chem. Soc.* **2022**, *144*, 10515.
[13] B. Sun, A. M. Najarian, L. K. Sagar, M. Biondi, M.-J. Choi, X. Li, L. Levina, S.-W. Baek, C. Zheng, S. Lee, A. R. Kirmani, R. Sabatini, J. Abed, M. Liu, M. Vafaie, P. Li, L. J. Richter, O. Voznyy, M. Chekini, Z.-H. Lu, F. P. García de Arquer, E. H. Sargent, *Adv. Mater.* **2022**, *34*, 2203039.
[14] J. Leemans, K. C. Dümbgen, M. M. Minjauw, Q. Zhao, A. Vantomme, I. Infante, C. Detavernier, Z. Hens, *J. Am. Chem. Soc.* **2021**, *143*, 4290.
[15] M. Soreni-Harari, D. Mocatta, M. Zimin, Y. Gannot, U. Banin, N. Tessler, *Adv. Funct. Mater.* **2010**, *20*, 1005.
[16] S. Tamang, C. Lincheneau, Y. Hermans, S. Jeong, P. Reiss, *Chem. Mater.* **2016**, *28*, 2491.
[17] J.-H. Ko, D. Yoo, Y.-H. Kim, *Chem. Commun.* **2017**, *53*, 388.
[18] K. Kim, D. Yoo, H. Choi, S. Tamang, J.-H. Ko, S. Kim, Y.-H. Kim, S. Jeong, *Angew. Chem.* **2016**, *128*, 3778.
[19] F. P. García de Arquer, A. Armin, P. Meredith, E. H. Sargent, *Nat. Rev. Mater.* **2017**, *2*, 16100.
[20] J. Kublitski, A. Hofacker, B. K. Boroujeni, J. Benduhn, V. C. Nikolis, C. Kaiser, D. Spoltore, H. Kleemann, A. Fischer, F. Ellinger, K. Vandewal, K. Leo, *Nat. Commun.* **2021**, *12*, 551.
[21] M. Burgelman, P. Nollet, S. Degrave, *Thin Solid Films* **2000**, *361*, 527.
[22] M. Burgelman, K. Decock, S. Khelifi, A. Abass, *Thin Solid Films* **2013**, *535*, 296.
[23] L. Shi, H. Yuan, X. Sun, X. Li, W. Zhu, J. Wang, L. Duan, Q. Li, Z. Zhou, Z. Huang, X. Ban, D. Zhang, *ACS Appl. Energy Mater.* **2021**, *4*, 10584.
[24] S. Yin, C. H. Y. Ho, S. Ding, X. Fu, L. Zhu, J. Gullett, C. Dong, F. So, *Chem. Mater.* **2022**, *34*, 5433.
[25] O. Voznyy, L. Levina, F. Fan, G. Walters, J. Z. Fan, A. Kiani, A. H. Ip, S. M. Thon, A. H. Proppe, M. Liu, E. H. Sargent, *Nano Lett.* **2017**, *17*, 7191.
[26] T. S. Bischof, R. E. Correa, D. Rosenberg, E. A. Dauler, M. G. Bawendi, *Nano Lett.* **2014**, *14*, 6787.
[27] R. H. Gilmore, Y. Liu, W. Shcherbakov-Wu, N. S. Dahod, E. M. Y. Lee, M. C. Weidman, H. Li, J. Jean, V. Bulović, A. P. Willard, J. C. Grossman, W. A. Tisdale, *Matter* **2019**, *1*, 250.
[28] N. Bouarissa, H. Aourag, *Infrared Phys. Technol.* **1999**, *40*, 343.
[29] R. J. Sladek, *Phys. Rev.* **1957**, *105*, 460.
[30] *Infrared Detectors* (Ed: A. Rogalski), CRC Press, Boca Raton **2010**.
[31] L. K. Sagar, G. Bappi, A. Johnston, B. Chen, P. Todorović, L. Levina, M. I. Saidaminov, F. P. García de Arquer, S. Hoogland, E. H. Sargent, *Chem. Mater.* **2020**, *32*, 2919.
[32] K. Lu, Y. Wang, Z. Liu, L. Han, G. Shi, H. Fang, J. Chen, X. Ye, S. Chen, F. Yang, A. G. Shulga, T. Wu, M. Gu, S. Zhou, J. Fan, M. A. Loi, W. Ma, *Adv. Mater.* **2018**, *30*, 1707572.
[33] S. a. R. Horsley, M. Artoni, G. C. La Rocca, *Nat. Photonics* **2015**, *9*, 436.
[34] M. Biondi, M. Choi, Z. Wang, M. Wei, S. Lee, H. Choubisa, L. K. Sagar, B. Sun, S. Baek, B. Chen, P. Todorović, A. M. Najarian, A. Sedighian Rasouli, D. Nam, M. Vafaie, Y. C. Li, K. Bertens, S. Hoogland, O. Voznyy, F. P. García de Arquer, E. H. Sargent, *Adv. Mater.* **2021**, *33*, 2101056.
[35] M. Vafaie, J. Z. Fan, A. Morteza Najarian, O. Ouellette, L. K. Sagar, K. Bertens, B. Sun, F. P. García de Arquer, E. H. Sargent, *Matter* **2021**, *4*, 1042.
[36] P. Yu, M. C. Beard, R. J. Ellingson, S. Ferrere, C. Curtis, J. Drexler, F. Luiszer, A. J. Nozik, *J. Phys. Chem. B* **2005**, *109*, 7084.
[37] G. Kresse, J. Furthmüller, *Phys. Rev. B* **1996**, *54*, 11169.
[38] J. P. Perdew, K. Burke, M. Ernzerhof, *Phys. Rev. Lett.* **1996**, *77*, 3865.
[39] J. Heyd, G. E. Scuseria, M. Ernzerhof, *J. Chem. Phys.* **2003**, *118*, 8207.
[40] J. Paier, M. Marsman, K. Hummer, G. Kresse, I. C. Gerber, J. G. Ángyán, *J. Chem. Phys.* **2006**, *124*, 154709.